To be published in Optical Materials Express:

Title: Flexible PAN-BiOI-AgI heterojunction nanofiber and the photocatalytic degradation property

Authors: pingping teng,Zhiang Li,Shuai GAO,Kang Li,Nigel Copner,Zhihai Liu,XINGHUA YANG

Accepted: 04 January 22

Posted 26 January 22

DOI: https://doi.org/10.1364/OME.450592

Flexible PAN-BiOI-AgI heterojunction nanofiber and the photocatalytic degradation property

Pingping Teng,[1] Zhiang Li,[1] Shuai Gao,[1,*] Kang Li,[2] Nigel Copner,[2] Zhihai Liu,[1] Xinghua Yang,[1] Enming Zhao,[3] Yu Zhang[1], Tao Geng,[1] and Fengjun Tian[1]

[1]*Key Laboratory of In-Fiber Integrated Optics, Ministry of Education, College of Science, Harbin Engineering University, Harbin 150001, China*
[2]*Wireless & Optoelectronics Research & Innovation Centre, Faculty of Computing, Engineering & Science, University of south Wales, Wales, CF371DL, UK*
[3]*School of Engineering, Dali University, Dali, China*
[4]*shuai.gao@hrbeu.edu.cn;*
[5]*liuzhihai@hrbeu.edu.cn*

Abstract: In this paper, the flexible polyacrylonitrile (PAN) nanofibers are used as carriers to prepare one-dimensional bismuth oxyiodide-silver iodide (BiOI-AgI) photocatalyst. PAN-BiOI-AgI is prepared on the surface of electrospun PAN nanofibers by alternate growth method and subsequent ion exchange method at room temperature. The results of XRD, TEM, XPS, and UV-Vis diffuse reflectance spectroscopy indicate the heterojunctions formation. The flexible PAN-BiOI-AgI heterojunction fibers show higher photocatalytic degradation efficiency for rhodamine B than PAN-BiOI or PAN-AgI. The enhanced photocatalytic performance is attributed to that the heterojunction improves the photo-generated electron-hole separation efficiency. After 60 min of visible light irradiation, the degradation efficiency is greater than 95%. Free radical capture experiments show that•O^{2-} and h+ are the main groups involved in the oxidation reaction.

1. Introduction

In the face of increasingly serious environmental pollution, the degradation of harmful substances in water bodies has received more and more attention [1-7]. Semiconductor photocatalysis, as an environmentally friendly green catalytic technology, can directly convert abundant solar energy into chemical energy, which is an effective way to deal with environmental pollution [8-15]. The use of solar energy to catalyze the degradation of pollutants is a practical way to deal with toxic organic matter to solve environmental pollution. In particular, bismuth-based oxide semiconductors have a wide visible light response range and good physical and chemical stability, and have become a frontier and hot spot in the field of photocatalytic materials research [16-22]. Among them, the indirect band gap semiconductor bismuth oxyhalide (BiOX, X = Cl, Br, I) materials have gradually become the focus of research due to their strong photochemical stability and suitable energy band position [23-27]. The transition of the indirect band gap semiconductor makes the photo-generated electrons in BiOX only pass through the k-space to transition back to the valence band, which greatly reduces the photo-generated carrier current. The recombination of electrons is beneficial to improve the separation efficiency of charges and the photocatalytic activity of the material. Bismuth halide (BiOI) has become an efficient new semiconductor photocatalytic material due to its unique electronic structure, layered atomic arrangement and visible light absorption properties [28,29]. BiOI has a narrow band gap of about 1.8 eV and strong absorption in the visible light region. It has attracted widespread attention. Due to the

morphology and structure of nano-flakes, BiOI has a high specific surface area and has higher visible light catalytic activity than bulk. However, due to the lack of effective carriers for such nano-sized catalysts, separation is difficult and may cause secondary pollution to the environment [30-32]. Moreover, due to the poor conductivity, the electron-hole carrier recombination probability of pure phase BiOI is high, which is not conducive to the oxidation-reduction reaction in the photocatalytic process.

Electrospinning technology is a simple and effective method to prepare one-dimensional nanofibers [36-38]. Electrospun fibers possess high specific surface area and have received extensive attention in the field of photocatalyst preparation. Specifically, electrospun fibers can be prepared using precursor solutions containing polymers as well as photocatalyst nanoparticles to act as photocatalysts. Alternatively, semiconductor heterojunctions can be prepared by combining high-temperature heat treatment and solvothermal methods to accomplish photocatalysis [39]. Compared with direct doping of catalysts for electrospinning, the method of growing photocatalysts on the surface of fiber-template is more beneficial to increase the catalyst loading. In particular, electrospun PAN nanofiber is a favourable nano-photocatalyst carrier because of its unique performance. Firstly, the electrospun PAN nanofibers possess the property of water-insoluble which enables the stability when they are immersed in water. Secondly, the one-dimensional fiber has a relatively high specific surface area and it fully contacts with the organic dyes in the water when it is immersed in water. Finally, the disordered fibers form a macroscopic network structure, and its flexibility is beneficial to the separation, recovery and reuse of the catalyst after the photodegradation. Therefore, electrospun PAN nanofibers improve the photodegradation efficiency, overcome the problem of agglomeration, and solve the difficulty of recycling.

In this paper, PAN nanofibers prepared by electrospinning method are used as carriers to grow BiOI nanosheets on their surface by alternate growth method, and then AgI nanoparticles are grown on BiOI surface by ion exchange method to form BiOI-AgI semiconductor photocatalytic heterojunctions. PAN-BiOI-AgI nanofibers show good photocatalytic degradation performance.

2. Experimental section

2.1. Preparation of PAN nanofibers

To prepare PAN precursor solution, 15 g of PAN (Mw=500000) as well as 100 mL N,N-dimethylformamide (DMF) were weighed and PAN powder was slowly added into DMF under stirring. The mixture was stirred magnetically for 24 h at 50 °C to dissolve sufficiently to form a transparent polymer solution. The air humidity was adjusted to 40% for electrospinning. The PAN solution was drawn into a 5 mL of syringe and 10 kV was applied, and the PAN nanofibers were received at the aluminum foil electrode with a receiving distance of 15 cm and an injection rate of 15 μL/min. The PAN fiber mats were collected after 48 h and dried in a vacuum drying oven at 50°C for 24 h.

2.2. Preparation of BiOI-loaded PAN nanofibers

The catalytic material was prepared on the surface of PAN nanofibers obtained in the previous step by using them as growth carriers. Alternate ion growth was performed by adsorbing Bi and I sources on the surface of PAN fibers to obtain BiOI nanospheres. Specifically, $Bi(NO_3)_3 \cdot 5H_2O$ and KI solutions with the same molar concentrations were prepared, respectively. 240 mg of $Bi(NO_3)_3 \cdot 5H_2O$ and 83 mg of KI were weighed and ultrasonically dissolved in 50 mL of ultrapure water to obtain solutions with a concentration of 10 mM, and the two solutions were labeled as solution 1 and solution 2, respectively. 100 mg of the above PAN electrospun sample was immersed in solution 1 and stirred magnetically for 5 min. The sample was then washed with ultrapure water to remove the free particles from the surface of PAN fiber. Afterwards, it was immersed into solution 2 and

stirred for 5 min. These three steps are one cycle. By adsorbing BiO^+ ions as well as I^- ions alternately, BiOI was generated on PAN surface. By controlling the different numbers of cycles, the loading amounts of BiOI on the PAN surface were adjusted. Here, the number of alternate growths was 5, 10 and 20. After growth, the fiber were washed with ethanol and dried in a vacuum drying oven at 60 °C. The samples were labeled as PB-1, PB-2 and PB-3.

2.3. Preparation of PAN-BiOI-AgI semiconductor heterojunction nanofibers

After finishing the growth of BiOI on the PAN surface, AgI nanoparticles were grown on the BiOI surface by ion exchange method. In order to control the AgI content, the final amount of BiOI-AgI deposited on the PAN fiber surface was controlled by adjusting the concentration of $AgNO_3$. Specifically, 1 mg, 2 mg, 4 mg and 8 mg of $AgNO_3$ were weighed and dissolved in 100 mL of ultrapure water to obtain different concentrations of $AgNO_3$ solution. The PAN-BiOI nanofibers prepared by the above method were immersed in the $AgNO_3$ solution and stirred for 6 h at room temperature. Ag^+ ions reacted with I^- ions in BiOI to generate AgI on the surface of BiOI. Four PAN-BiOI-AgI samples generated under different Ag^+ concentration were labeled as PBA-1, PBA-2, PBA-3, and PBA-4, and were used for visible light catalysis experiments.

2.4. Photocatalytic degradation

To characterize the catalytic properties of the photocatalyst, photocatalytic experiment of dye degradation was carried out. A 150 W xenon lamp was employed as the light source and a visible light filter (>420 nm) was placed at the light exit of the xenon lamp. RhB was used as the photocatalytic object and its aqueous solution concentration was 10 mg/L. Specifically, 100 mg of photocatalytic fiber was weighed and placed in 50 mL of RhB solution. It was stirred in the dark for 30 min to reach adsorption equilibrium. Then, photocatalysis was carried out under light radiation while stirring. Every 10 minutes, 4 mL of solution was removed and centrifuged, and the absorbance at the wavelength of 554 nm was measured.

3. Results and discussion

3.1. Structure characterization of the samples

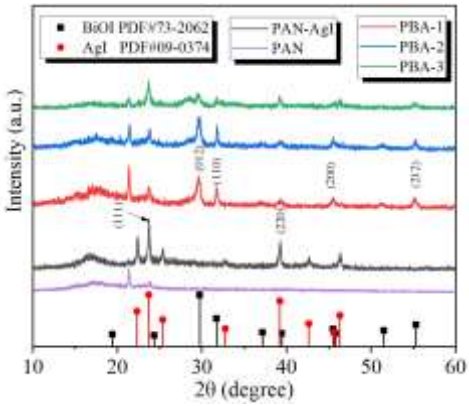

Fig. 1. X-ray powder diffraction pattern of different samples.

The XRD spectra of the PAN-loaded photocatalysts are given in Fig. 1. Compared to the bare PAN fibers, PBA-1, PBA-2, PBA-3 all show the main characteristic peaks of BiOI, located at 29.71º, 31.72º, 45.51º and 55.26º, respectively. These peaks correspond to the (012), (110), (200) and (212) crystal planes of BiOI, respectively (PDF Card No. 73-2062). As in the PAN-AgI sample, two main peaks at 23.78º and 39.26º were also observed in PBA-1, PBA-2, and PBA-3, corresponding to the (111) and (220) crystal planes of AgI (PDF Card No. 09-0374), respectively. With the increase of AgI loading, BiOI is gradually covered by AgI and the

intensity of the characteristic peaks of BiOI gradually decreases. Meanwhile, the diffraction peaks of AgI gradually increase. The above results indicate that crystalline BiOI and AgI are loaded on the surface of the PAN fiber.

3.2. Morphologies and element distribution

The morphology of the fibers with different photocatalysts grown on the surface is shown in Fig. 2. The morphologies of PAN-BiOI samples (PB-1, PB-2 and PB-3) grown on the PAN surface with different number of cycles are given in Fig. 2(a)-(c). From the figures, it can be seen that nanocrystals with different sizes are grown on the PAN fiber surface, which is originally smooth with a diameter of about 200 nm. However, the morphology of the fibers and the amount of loaded BiOI varied greatly with the increase of the number of cycles. When the number of growths is 5, a small amount of granular BiOI is faintly visible on the surface, but with further growths, the loading of BiOI on the surface gradually increases and flake morphology is gradually formed. At the same time, the overall diameter of the fibers gradually increased with the increase of BiOI loading. As can be seen in Fig. 2(c), the PAN surface carries a large number of flake stacked BiOI nanosheets with a size of about 500 nm (inset). The flake BiOI loaded on the fiber surface provides the photocatalyst a large specific surface area. Further, after the ion-exchange reaction on the PAN-BiOI surface, the morphology of the flake BiOI was change. From Fig. 2(d), it can be seen that AgI nanocrystals were precipitated on the BiOI surface and the color of the fiber changed from brown to pale yellow. This can also be demonstrated later in the elemental analysis.

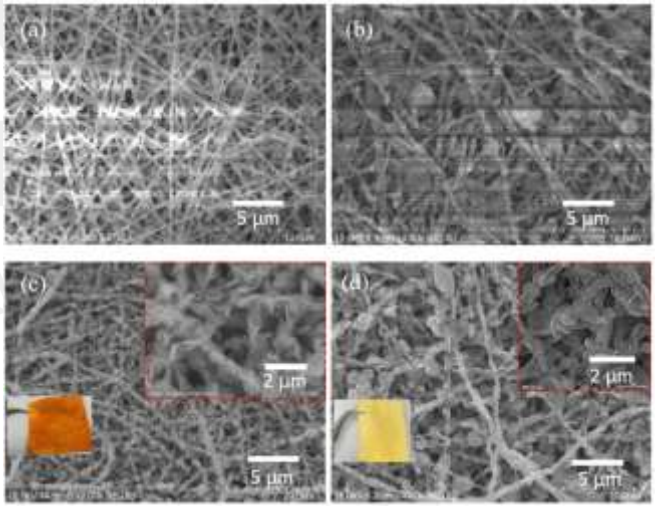

Fig. 2. SEM images of the PAN-BiOI fibers with different alternate growing cycles and the fibers after growth of AgI (a) PB-1 (b) PB-2 (c) PB-3 (d) PBA-3.

The SEM image of PBA-3 and the elemental distribution are given in Fig. 3. Fig. 3(b)-(e) correspond to the distributions of Bi, O, I, and Ag elements within the area of Fig. 3(a), respectively. As can be seen from the figures, the uniform distribution of Bi, O, and I elements indicates that the flakes generated on the PAN surface are BiOI. As shown in Fig. 3(e), Ag element is uniformly distributed within the scanned area. According to Fig. 3(b)-(e), the homogenous distribution of elements is proved. Fig. 3(f) gives the energy-dispersive X-ray (EDX) spectra of PBA-3 and also proves the existence of Bi, O, I, and Ag. The atom ratio of Ag and Bi is 0.276:1 according to the quantitative analysis of EDX.

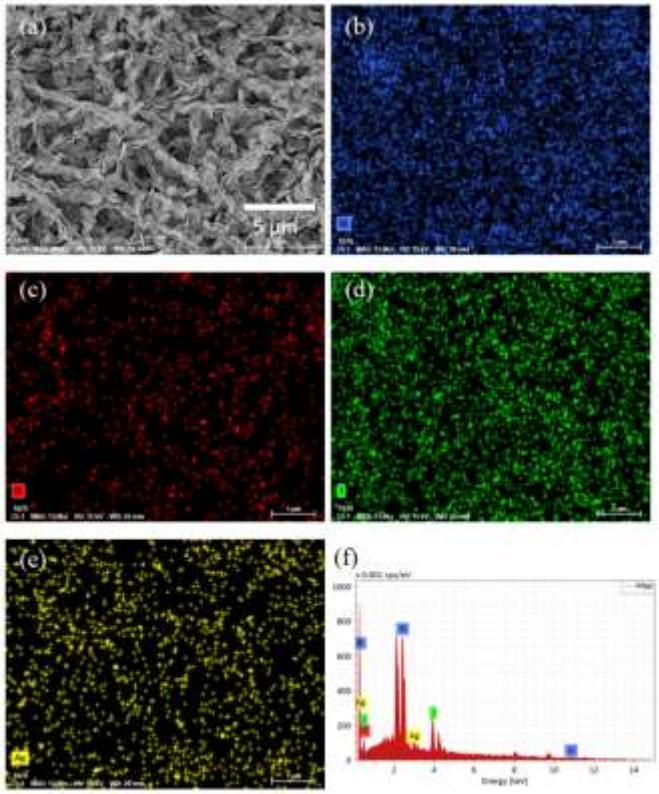

Fig. 3. SEM image and surface scan elemental mapping of PBA-3 (a)SEM image (b)Bi (c) O (d) I (e) Ag (f) EDX spectra.

To further demonstrate the growth of AgI on the surface of BiOI, TEM characterization was performed on the crushed PBA-3 samples. Fig. 4(a) shows the dark field image of a local range. Fig. 4(b)-(f) show the distribution analysis of C, I, Bi, O, and Ag elements. The distribution of C on the fiber in Fig. 4(b) is caused by C in the PAN material. The other elemental distributions in Fig. 4(c)-(f) demonstrate the presence of BiOI as well as AgI. In Fig. 4(f), Ag element shows stronger intensity in some areas (e.g., bottom left corner), but Bi element shows much lower intensity in the same area. This is the evidence that there are AgI growth points on the surface of BiOI flakes.

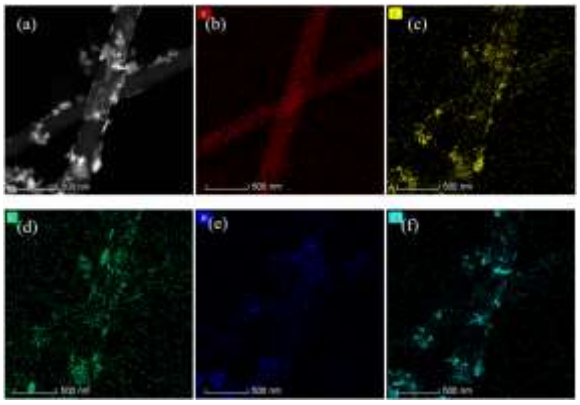

Fig. 4. Local area dark-field TEM image and surface scanning element analysis. (a) Dark-field TEM image (b) C (c) I (d) Bi (e) O (f) Ag.

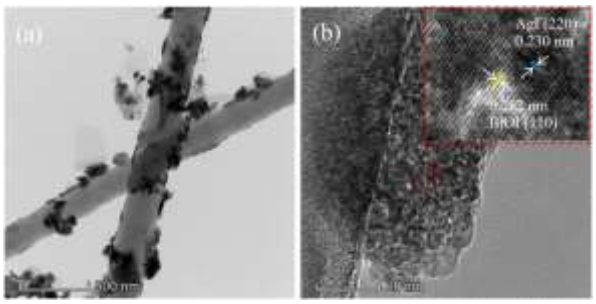

Fig. 5. HRTEM analysis of PBA-3 sample with heterojunction semiconductor structure (a) Bright-field TEM image (b) lattice structure of heterojunction.

Bright-field high-resolution transmission electron microscopy (HRTEM) images of the discrete PBA-3 fibers of the crushed sample are given in Fig. 5. The retained nanoparticles on the surface of PAN fiber in Fig. 5(a) was selected as the analysis point. Two different lattice fingerprints are observed in Fig. 5(b) with lattice spacing of 0.282 nm and 0.230 nm for BiOI and AgI, corresponding to the crystalline planes (110) and (220), respectively. This indicates the formation of BiOI and AgI heterojunctions on PAN fiber surface. The formation of heterojunctions is attributed to the surface growth reaction of Ag^{+} ions capturing I^{-} ions from BiOI and thus generating AgI.

3.3. Chemical composition and electronic state of the photocatalyst

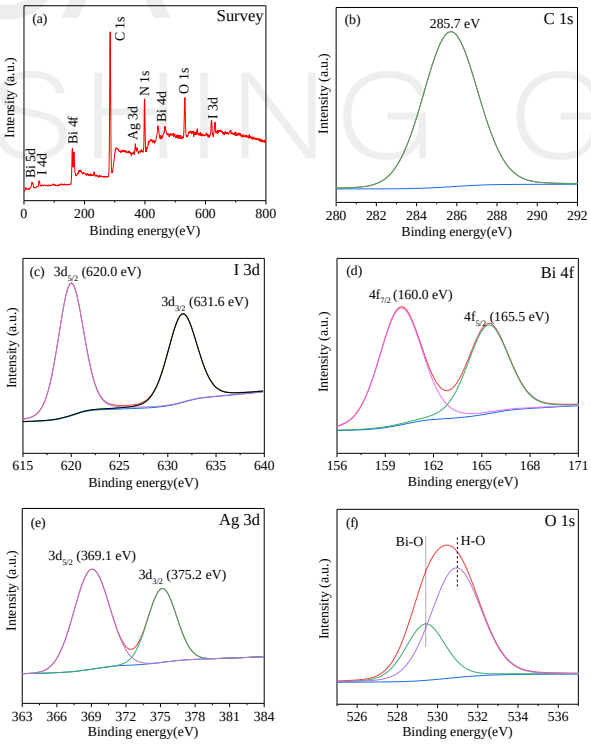

Fig. 6. X-ray photoelectron spectra of PBA-3 sample (a) Full survey spectrum (b) C 1s (c) I 3d (d) Bi 4f (e) Ag 3d (f) O 1s

As shown in Fig. 6, the X-ray photoelectron spectra (XPS) of PBA-3 fiber were studied in order to characterize the chemical composition and electronic states of the materials on the

surface of PAN fiber. The full survey spectrum is given in Fig. 6(a). Bi, O, I, C, N, and Ag elements are observed in it. This is in accordance with the composition of PAN-BiOI-AgI. Fig. 6(b)-(f) show the XPS spectra of C 1s, I 3d, Bi 4f, Ag 3d, and O 1s, respectively. Fig. 6(b) shows the main peak of C 1s located at 285.7 eV, which is used to calibrate with the standard peak of C 1s at 284.6 eV. This C peak is caused by the PAN fiber. Fig. 6(c) shows two peaks at 620.0 eV and 631.6 eV which are attributed to I $3d_{5/2}$ and I $3d_{3/2}$, respectively, corresponding to the I^- ions[40]. The peaks of 160.0 eV and 165.5 eV in Fig. 6(d) correspond to Bi $4f_{7/2}$ and Bi $4f_{5/2}$, which are attributed to Bi^{3+}[22]. The peaks of 369.1 eV and 375.2 eV in Fig. 6(e) correspond to Ag $3d_{5/2}$ and Ag $3d_{3/2}$, respectively, which indicate the presence of Ag^+ [41]. Finally, the XPS spectra of O 1s in Fig. 6(f) are non-single peaks. This indicates that there is more than one chemical state of O in it. The peak at 529.4 eV corresponds to the lattice oxygen negative ion, corresponding to the Bi-O bond of $[Bi_2O_2]$ in the BiOI layer. And another one near 531.0 eV indicates the presence of -OH or adsorbed O on the fiber surface [42]. The above results demonstrate the chemical valence states of various elements in PAN-BiOI-AgI.

The optical absorption properties of the different photocatalyst samples were characterized by UV-vis diffuse reflectance spectroscopy as shown in Fig. 7(a). From the figure, all the photocatalysts exhibit strong optical absorption in the visible wavelength range. Among them, the absorption band edge of PB-3 fibers loaded with BiOI on PAN surface is larger than 600 nm, indicating a narrow band gap. In contrast, the absorption band edge of the PAN-AgI sample directly loaded with AgI on PAN surface is located at a shorter wavelength position (~470 nm), indicating a wide band gap. Further, when AgI was loaded on the surface of PAN-BiOI, the absorption band edge of the PBA-3 fibers significantly shifted to a shorter wavelength, indicating that a heterojunction was formed between the them. This contributes to the further separation of photo-generated electron and holes in BiOI. The semiconductor band gap of a photocatalytic material can be calculated by $\alpha h\nu = A(h\nu - E_g)^{n/2}$, where α, E_g, A, h, ν are the optical absorption coefficient, band gap width, proportionality constant, Planck's constant, and frequency, respectively. For direct bandgap semiconductors, where n=1, and for indirect bandgap semiconductors, n=4 [41]. Here, AgI is a direct bandgap semiconductor and n takes the value of 1, and BiOI is an indirect bandgap semiconductor and n takes the value of 4. Therefore, to obtain the bandgap values, PAN-BiOI and PAN-AgI should correspond to $h\nu\text{-}(\alpha h\nu)^{1/2}$ and $h\nu\text{-}(\alpha h\nu)^2$ for plotting, respectively. As shown in Fig. 7(b), the band gap value can be determined by the intersection of the horizontal axis with the tangent line of the curve. In the graph, it is seen that the band gaps of PAN-AgI and PB-3 are 2.75 eV and 1.89 eV, respectively. The band gap of PBA-3 which is a composite of both components lies between PAN-AgI and PB-3. This indicates the formation of heterojunctions between them, which is easier to obtain photo-generated carriers.

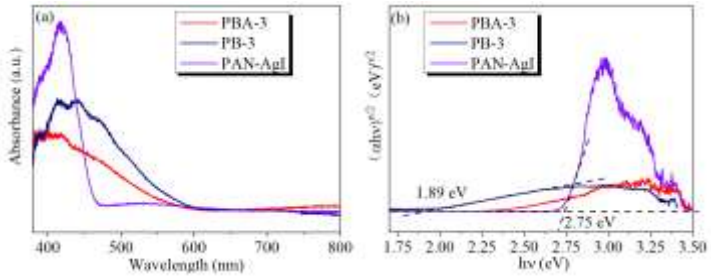

Fig. 7. (a) UV-Vis diffuse reflectance spectra of PAN-BiOI-AgI, PAN-BiOI and PAN-AgI samples (b) $h\nu\text{-}(\alpha h\nu)^{n/2}$ curves of the samples.

The valence band potential and conduction band potential of a semiconductor photocatalyst can be calculated by the following formula [44]:

$$E_{VB} = X - E_e + 0.5E_g$$

$$E_{CB} = E_{VB} - E_g$$

Among them, E_{VB} is the top of the valence band of the semiconductor, X is the electronegativity of the semiconductor, E_g is the forbidden band width of the semiconductor, and E_e is the surface electron free energy of hydrogen atoms. Here, E_e is 4.5 eV, and the X values of BiOI and AgI are 5.94 eV and 5.35 eV, respectively. Since the E_g values of PAN-AgI and PB-3 are 2.75 eV and 1.89 eV, respectively, the E_{VB} values of PAN-AgI and PB-3 are 2.23 eV (vs. NHE) and 2.39 eV (vs. NHE) after putting the constants into the formula. In addition, according to the conversion relationship between the conduction band and the valence band, $E_{CB} = E_{VB} - E_g$, the E_{CB} values of PAN-AgI and PB-3 can be obtained as -0.53 eV (vs. NHE) and 0.49 eV (vs. NHE), respectively.

3.4. Catalytic performance and catalytic mechanism of the photocatalyst

Fig. 8(a) indicates the dark reaction and the performance of photocatalytic degradation. After 30 min of adsorption in the dark, the visible irradiation starts. During the period of -30 min~10 min, it is shown that PAN-AgI has a stronger adsorption than PB-3, but the degradation rate of PAN-AgI is lower than PB-3 after starting light irradiation, so the degradation curves of PAN-AgI and PB-3 intersect. The photocatalytic degradation performance in the time period from 0 min to 60 min is shown. The degradation rates of BiOI-loaded PB-3 fiber and AgI-loaded PAN-AgI fiber are 73.4% and 55.1% at 60 min, respectively. When AgI was loaded on the BiOI surface, the degradation rates of PBA-1, PBA-2, PBA-3, and PBA-4 all increased significantly, and the photocatalytic efficiency of PBA-3 was closed to 100% at 60 min. The degradation rate of PBA-3 is significantly higher than that of PB-3. Fig. 8(b) shows the kinetic analysis of the degradation reaction. The results show that the photocatalytic degradation conforms to the Langmuir-Hinshelwood first-order apparent kinetic model [45]:

$$\mathrm{r} = \frac{\mathrm{dC}}{\mathrm{dt}} = kk{\cdot}C/(1 + k{\cdot}C)$$

Here, r is the degradation rate (mg $L^{-1}h^{-1}$), C is the residual concentration (mg L^{-1}), t is the degradation time (h), k is the reaction constant (mg $L^{-1}h^{-1}$), $k'$is the absorption coefficient (L mg^{-1}). Due to the low initial concentration of the dye, the above equation can be approximated to a first-order form:

$$-\ln\left(\frac{C}{C_0}\right) = kk{\cdot}t = k_{app}t$$

Where C_0 is the concentration at adsorption equilibrium and k_{app} is the slope that is also the reaction constant. As shown in Fig 8(b), the k_{app} values of PB-3, PAN-AgI, PBA-1, PBA-2, PBA-3, and PBA-4 are 0.018 min^{-1}, 0.007 min^{-1}, 0.025 min^{-1}, 0.036 min^{-1}. 0.072 min^{-1} and 0.048 min^{-1}, respectively. The photocatalytic constants of PBA-3 are 4 times and 10.3 times that of PB-3 and PAN-AgI, respectively. This shows the heterojunctions formed by BiOI and AgI on the PAN surface effectively improve the electron-hole separation efficiency and the photocatalytic rate. In order to test the reusability of the photocatalyst, four cycles of photocatalytic experiments were performed on PBA-3. From Fig. 8(c), it is seen that the photocatalytic performance did not decrease significantly after repeated photocatalytic degradation of the solution with the same concentration. The final degradation rate decay was less than 10%, indicating that the modified fiber can be reused.

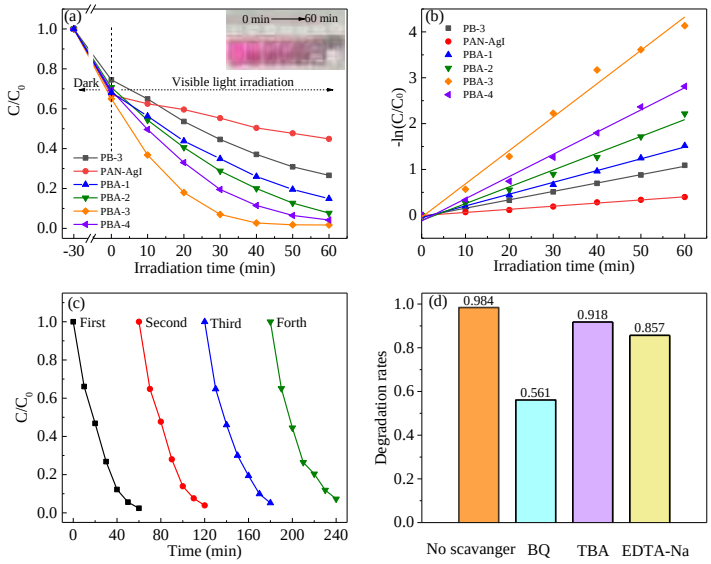

Fig. 8. Photocatalytic degradation of RhB (a) Degradation curves of RhB by different catalysts of PB-3, PAN-AgI, PBA-1, PBA-2, PBA-3, and PBA-4 (inset: photograph of actual degradation process of RhB by PBA-3) (b) Linear fitting of first order kinetics of degradation process of PB-3, PAN-AgI, PBA-1, PBA-2, PBA-3, and PBA-4 (c) The cyclic degradation experiment of PBA-3. (d) The influence of different trapping agents on the degradation efficiency of PBA-3.

The photocatalytic mechanism of electrospun fibers loaded with BiOI-AgI was investigated. The internally generated photoactive groups were determined by adding different types of capturing agents in the catalytic system. The type of specific active groups was determined by the degree of photocatalytic activity reduction. Fig. 8(d) shows that the addition of p-benzoquinone (BQ), EDTA-2Na, and tert-butanol (TBA) to the system affected the degradation rate to different degrees, respectively. BQ, EDTA-2Na, and TBA reduced the degradation rate to 0.561, 0.918, and 0.857 of the original rate within 60 min, respectively. It is seen that a large amount of O^{2-} and a small amount of ·OH and h^+ were produced on the photocatalyst surface.

As shown in Fig. 9, when the photocatalyst is irradiated by visible light, BiOI and AgI on the PAN surface are excited and electrons jump from the valence band to the conduction band. Since the conduction band potential of AgI (-0.53 eV) is more negative than that of $O_2/·O^{2-}$(-0.33 eV) potential, the electrons reduce the O_2 in water and produce the reactive group $·O^{2-}$ to degrade RhB. Meanwhile, because the conduction band potential of AgI is also more negative than that of BiOI (0.49 eV), the photo-generated electrons migrate to the conduction band of BiOI. Because the valence band potential of BiOI (2.39 eV) is more positive than that of AgI (2.23 eV), the h^+ of BiOI migrate to the valence band of AgI, thus forming a carrier cycle and also avoiding the electron reduction of AgI to produce Ag. Then, h^+ generated from the valence band of AgI also partially mineralizes and degrades RhB. Because the VB value of BiOI is 2.39 eV, which is slightly higher than the $OH^-/·OH$ oxidation potential of 2.38 eV, a small amount of ·OH is produced in the system.

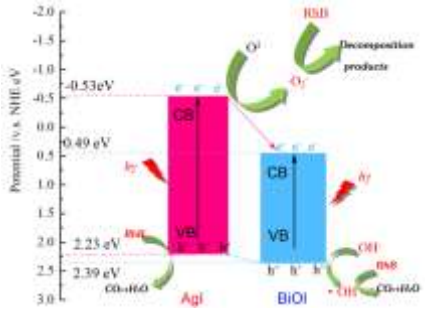

Fig. 9 The mechanism of photo-generated electron-hole separation, transfer and photocatalytic reaction.

4. Conclusion

By cyclic growth and ion exchange methods, BiOI-AgI semiconductor photocatalytic heterojunctions are successfully loaded on the surface of electrospun PAN nanofibers. The results of morphological characterization and elemental analysis show the photocatalysts are loaded on the fiber surface in the form of flakes, and the loaded fiber possesses high specific surface area and uniform elemental distribution. HRTEM, XRD and XPS results indicate that the physical phases on the fiber surface are BiOI and AgI, and heterojunctions are formed between them. The results of visible light photocatalytic experiments demonstrate that the photocatalytic efficiency of BiOI-AgI heterojunctions is significantly higher than that of the single components. The mechanism analysis illustrates that a large amount of $\cdot O^{2-}$ is generated in the photocatalytic system, which plays the major role, while $\cdot OH$ and h^+ play a supporting role. By adjusting the ion exchange concentration, PAN-BiOI-AgI photocatalyst is able to completely degrade RhB solution with a concentration of 10 mg/L within 60 min. The formation of heterojunctions significantly improves the separation of photo-generated electron-hole. Moreover, no significant degradation of the photocatalyst performance occurs after four cycles of photocatalytic experiments. In conclusion, this photocatalytic BiOI-AgI loaded nanofiber based on electrospinning not only forms heterojunctions and possesses a high specific surface area to improve photocatalytic efficiency, but also its flexibility facilitates separation and recycling.

5. Funding

National Natural Science Foundation of China (11574061, 62065001; 61975039; 62175046); Fundamental Research Funds for the Central Universities (3072021CF2517; 3072021CF2509); National Key R&D Program of China (2018YFC1503703); Natural Science Foundation of Heilongjiang Province (LH2021F019).

Disclosures

The authors declare no conflicts of interest.

Data availability

Data underlying the results presented in this paper are not publicly available at this time but may be obtained from the authors upon reasonable request.

References

1. J. A. Downing, S. Polasky, S. M. Olmstead, and S. C. Newbold, "Protecting local water quality has global benefits," Nat. Commun. **12**, 2709 (2021).
2. P. Bonetti, C. Leuz, and G. Michelon, "Large−sample evidence on the impact ofunconventional oil and gas development onsurface waters," Science **373**, 896−902 (2021).

3. M. Ashraf, I. Khan, M. Usman, A. Khan, S. S. Shah, A. Z. Khan, K. Saeed, M. Yaseen, M. F. Ehsan, M. N. Tahir, and N. Ullah, “Hematite and magnetite nanostructures for green and sustainable energy harnessing and environmental pollution control: a review,” Chem. Res. Toxicol. **33**, 1292−1311 (2020).
4. Y. Ye, Y. Zhang, Y. Zhao, Y. Ren, and X. Ren, “Sensitivity influencing factors during pesticide residue detection research via a terahertz metasensor,” Opt. Express **29**, 15255−15268 (2021).
5. A. Mukherjee, A. Satish, A. Mullick, J. Rapolu, S. Moulik, A. Roy, and A. K. Ghosh, “Paradigm shift toward developing a zero liquid discharge strategy for dye−contaminated water streams: a green and sustainable approach using hydrodynamic cavitation and vacuum membrane distillation,” ACS Sustainable Chem. Eng. **9**, 6707−6719 (2021).
6. M. S. Bank, P. W. Swarzenski, C. M. Duarte, M. C. Rillig, A. A. Koelmans, M. Metian, S. Wright, J. F. Provencher, M. Sanden, A. Jordaan, M. Wagner, M. Thiel, and Y. S. Ok, “Global plastic pollution observation system to aid policy,” Environ. Sci. Technol. **55**, 7770−7775 (2021).
7. Y. Feng, X. Chen, Y. Li, H. Zhao, L. Xiang, H. Li, Q. Cai, N. Feng, C. Mo, and M. Wong, “A visual leaf zymography technique for the in situ examination of plant enzyme activity under the stress of environmental pollution,” J. Agric. Food Chem. **68**, 14015−14024 (2020).
8. Q. Huang, T. D. Canady, R. Gupta, N. Li, S. Singamaneni, and B. T. Cunningham, “Enhanced Plasmonic Photocatalysis through Synergistic Plasmonic−Photonic Hybridization,” ACS Photonics **7**, 1994−2001 (2020).
9. Y. Lin, C. Yang, S. Wu, X. Li, Y. Chen, and W. Yang, “Construction of Built−In Electric Field within Silver Phosphate Photocatalyst for Enhanced Removal of Recalcitrant Organic Pollutants,” Adv. Funct. Mater. **30**(38), 2002918 (2020).
10. J. Ma, Q. Wang, L. Li, X. Zong, H. Sun, R. Tao, and X. Fan, “Fe_2O_3 nanorods/CuO nanoparticles p−n heterojunction photoanode: Effective charge separation and enhanced photoelectrochemical properties,” J. Colloid Interf. Sci. **602**, 32−42 (2021).
11. P. Zhou, J. Yu, and M. Jaroniec, “All−solid−state Z−scheme photocatalytic systems,” Adv. Mater. **26**, 4920−4935 (2014).
12. H. Wang, L. Zhang, Z. Chen, J. Hu, S. Li, Z. Wang, J. Liu, and X. Wang, “Semiconductor heterojunction photocatalysts: design, construction, and photocatalytic performance,” Chem. Soc. Rev. **43**, 5234−5244 (2014).
13. Q. Jiang, M. Z. Liu, C. L. Shao, X. W. Li, H. Y. Liu, X. H. Li, and Y. C. Liu, “Nitrogen doping polyvinylpyrrolidone−based carbon nanofibers via pyrolysis of g−C_3N_4 with tunable chemical states and capacitive energy storage,” Electrochim. Acta **330**, 135212 (2020).
14. F. Xu, B. Zhu, B. Cheng, J. Yu, and J. Xu, “1D/2D TiO_2/MoS_2 hybrid nanostructures for enhanced photocatalytic CO_2 reduction,” Adv. Opt. Mater. **23**(6), 1800911 (2018).
15. X. Yuan, S. L. Qu, X. Y. Huang, X. G. Xue, C. L. Yuan, S. W. Wang, L. Wei, and P. Cai, “Design of core−shelled g−C_3N_4@ZIF−8 photocatalyst with enhanced tetracycline adsorption for boosting photocatalytic degradation,” Chem. Eng. J. **416**, 129148 (2021).
16. S. Chen, D. Huang, P. Xu, X. Gong, W. Xue, L. Lei, R. Deng, J. Li, and Z. Li, “Facet−Engineered Surface and Interface Design of Monoclinic Scheelite Bismuth Vanadate for Enhanced Photocatalytic Performance,” ACS Catal. **10**(2), 1024−1059 (2020).
17. Y. Bao, W. J. Lee, J. Z. Y. Seow, H. Hara, Y. Liang, H. Feng, J. Z.C. Xu, T. T. Lim, and X. Hu, “One−Step Block Copolymer Templated Synthesis of Bismuth Oxybromide for Bisphenol A Degradation: An Extended Study from Photocatalysis to Chemical Oxidation,” ACS ES T Water **1**(4), 837−846 (2021).
18. L. Yao, Z. Chen, Z. Lu and X. Wang, “Plasmonic Bi metal as a co−catalyst deposited on C−doped $Bi_6O_6(OH)_3(NO_3)_3{\cdot}1.5H_2O$ for efficient visible light photocatalysis,” J. Photochem. Photobiol. A−Chem. **389**(15), 112290 (2020).
19. O. Monfort, G. Plesch, “Bismuth vanadate−based semiconductor photocatalysts: a short critical review on the efficiency and the mechanism of photodegradation of organic pollutants,” Environ. Sci. Pollut. Res. **25**, 19362−19379 (2018).
20. L. Yao, H. Yang, Z. Chen, M. Qiu, B. Hu, and X. Wang, “Bismuth oxychloride−based materials for the removal of organic pollutants in wastewater,” Chemosphere **273**, 128576 (2021).
21. X. Liao, X. Lan, N. Ni, P. Yang, Y. Yang, and X. Chen, “Bismuth Oxychloride Nanowires for Photocatalytic Decomposition of Organic Dyes,” ACS Appl Nano Mater **4**(4), 3887−3892 (2021).
22. P. P Teng, Z. A. Li, S. Gao, K. Li, M. Bowkett, N. Copner, Z. Liu, and X. Yang, “Fabrication of one−dimensional Bi_2WO_6/$CuBi_2O_4$ heterojunction nanofiber and its photocatalytic degradation property,” Opt. Mater. **121**, 111508 (2021).
23. S. Bao, H. Liang, C. Li, and J. Bai, “A heterostructure BiOCl nanosheets/TiO_2 hollow−tubes composite for visible light−driven efficient photodegradation antibiotic,” J. Photochem. Photobiol. A **397**, 112590 (2020).
24. D. Liu, D. Chen, N. Li, Q. Xu, H. Li, J. He, and J. Lu, “Surface Engineering of g−C_3N_4 by Stacked BiOBr Sheets Rich in Oxygen Vacancies for Boosting Photocatalytic Performance,” Angew. Chem. Int. Ed. **11**(59), 4519−4524 (2020).
25. F. Chen, H. Liu, S. Bagwasi, X. Shen, and J. Zhang, “Photocatalytic study of BiOCl for degradation of organic pollutants under UV irradiation,” J. Photochem. Photobiol. A **215**, 76−80 (2010).
26. H. Cheng, B. Huang, and Y. Dai, “Engineering BiOX (X = Cl, Br, I) nanostructures for highly efficient photocatalytic applications,” Nanoscale **6** (4), 2009−2026 (2014)

27. H. Wu, C. Yuan, R. Chen, J. Wang, F. Dong, J. Li, and Y. Sun, "Mechanisms of Interfacial Charge Transfer and Photocatalytic NO Oxidation on BiOBr/SnO_2 p–n Heterojunctions," ACS. Appl. Mater. Inter. **12** (39), 43741−43749 (2020).
28. S. Rieger, T. Fürmann, J. K. Stolarczyk, and J. Feldmann, "Optically Induced Coherent Phonons in Bismuth Oxyiodide (BiOI) Nanoplatelets," Nano Lett. **21** 7887−7893 (2021).
29. H. Zhu, C. Wang, X. Xiao, Z. Chen, Y. Wang, S. Xiao, Y. Li, and J. He, "Ultrafast saturable absorption of BiOI nanosheets prepared by chemical vapor transport," Opt. Lett. **46**(23), 6006−6009 (2021).
30. M. O. Olagunju, E. M. Zahran, J. M. Reed, E. Zeynaloo, D. Shukla, J. L. Cohn, B. Surnar, S. Dhar, L. G. Bachas, and M. R. Knecht, "Halide Effects in $BiVO_4$/BiOX Heterostructures Decorated with Pd Nanoparticles for Photocatalytic Degradation of Rhodamine B as a Model Organic Pollutant," ACS Appl. Nano Mater. **4**(3), 3262−3272 (2021).
31. X. Liao, X. Lan, N. Ni, P. Yang, Y. Yang, and X. Chen, "Bismuth Oxychloride Nanowires for Photocatalytic Decomposition of Organic Dyes," ACS Appl. Nano Mater. **4**(4), 3887−3892 (2021).
32. M. Arumugam, M. Y. Choi, "Recent progress on bismuth oxyiodide (BiOI) photocatalyst for environmental remediation," J. Ind. Eng. Chem. **81**, 237−268 (2020).
33. E. M. Akinoglu, D. A. Hoogeveen, C. Cao, A. N. Simonov, and J. J. Jasieniak, "Prospects of Z−Scheme Photocatalytic Systems Based on Metal Halide Perovskites," ACS Nano **15**(5), 7860−7878 (2021).
34. H. Guo, C. Niu, L. Zhang, X. Wen, C. Liang, X. Zhang, D. Guan, N. Tang, and G. Zeng, "Construction of Direct Z−Scheme AgI/$Bi_2Sn_2O_7$ Nanojunction System with Enhanced Photocatalytic Activity: Accelerated Interfacial Charge Transfer Induced Efficient Cr(VI) Reduction, Tetracycline Degradation and Escherichia coli Inactivation," ACS Sustain. Chem. Eng. **6**(6), 8003–8018 (2018).
35. A. Shoja, A. Habibi−Yangjeh, M. Mousavi, and S. Vadivel, "Preparation of novel ternary TiO_2 QDs/CDs/AgI nanocomposites with superior visible−light induced photocatalytic activity," J. Photochem. Photobiol. A−Chem. **385**, 112070 (2019).
36. S. Ponce−Alcántara, D. Martín−Sánchez, A. Pérez−Márquez, J. Maudes, N. Murillo, and J. García−Rupérez, "Optical sensors based on polymeric nanofibers layers created by electrospinning," Opt. Mater. Express **8**(10), 3163−3175 (2018).
37. Y. Sun, Y. Liu, Y. Zheng, Z. Li, J. Fan, L. Wang, X. Liu, J. Liu, and W. Shou, "Enhanced Energy Harvesting Ability of ZnO/PAN Hybrid Piezoelectric Nanogenerators," ACS Appl. Mater. Inter. **12**(49), 54936–54945 (2020).
38. X. Y. Huang, X. Zhang, K. X. Zhang, X. G. Xue, J. Xiong, Y. Huang, D. D. Zhang, J. Zhang, Z. L. Zhang, and F. P. Yan, "Defect-mediated Z-scheme carriers' dynamics of C-ZnO/A-CN toward highly enhanced photocatalytic TC degradation," J. Alloy. Compound. **877**(5), 160321 (2021).
39. H. Y. Liu, C. H. Han, C. L. Shao, S. Yang, X. W. Li, B. Li, X. H. Li, J. G. Ma, and Y. C. Liu, "ZnO/$ZnFe_2O_4$ Janus Hollow Nanofibers with Magnetic Separability for Photocatalytic Degradation of Water−Soluble Organic Dyes," ACS Appl. Nano Mater. **2**(8), 4879−4890 (2019).
40. Z. Liu, W. Xu, J. Fang, X. Xu, S. Wu, X. Zhu, and Z. Chen, "Decoration of BiOI quantum size nanoparticles with reduced graphene oxide in enhanced visible−light−driven photocatalytic studies," Appl. Surf. Sci. **259**(15), 441−447 (2012).
41. J. Choi, D. A. Reddy, and T. K. Kimn, "Enhanced photocatalytic activity and anti−photocorrosion of AgI nanostructures by coupling with graphene−analogue boron nitride nanosheets," Ceram. Int. **41**(10), 13793−13803 (2015).
42. A. Phuruangrat, P. Dumrongrojthanath, S. Thongtem, and T. Thongtem, "Hydrothermal synthesis of I−doped Bi_2WO_6 for using as a visible−light−driven photocatalyst," Mater. Lett. **224**, 67−70 (2018).
43. V. O. Odhiambo, C. R. M. Mustafa, L. B. Thong, Z. Kónya, and I. M. Szilágyi, "Preparation of TiO_2/WO_3/C/N composite nanofibers by electrospinning using precursors soluble in water and their photocatalytic activity in visible light," Nanomaterials **11**, 351 (2021).
44. D.A. Reddy, S. Lee, J. Choi, S. Park, R. Ma, H. Yang, and T. K. Kim, "Green synthesis of AgI−reduced graphene oxide nanocomposites: toward enhanced visible−light photocatalytic activity for organic dye removal," Appl. Surf. Sci. **341**, 175−184 (2015).
45. X. Zhang, C.L. Shao, X. Li, N. Lu, K. Wang, F. Miao, and Y. Liu, "In_2S_3/carbon nanofibers/Au ternary synergetic system: hierarchical assembly and enhanced visible−light photocatalytic activity," J. Hazard. Mater. **283**, 599−607 (2015).